A&A 671, A77 (2023)
https://doi.org/10.1051/0004-6361/202245207

Astronomy & Astrophysics

Compositional indication of E- and M-type asteroids by VIS-NIR reflectance spectra of meteorites

Pengfei Zhang (张鹏飞)[1,6], Yang Li (李阳)[2,7], Jiang Zhang (张江)[3], Shijie Li (李世杰)[2,7], Ziliang Jin (金子梁)[1,6], Huijie Han (韩慧杰)[4], Changqing Liu (刘长卿)[3], Yangting Lin (林杨挺)[5], Zongcheng Ling (凌宗成)[3], and Yuanyun Wen (文愿运)[2]

[1] State Key Laboratory of Lunar and Planetary Sciences, Macau University of Science and Technology, Macao, PR China
[2] Center for Lunar and Planetary Sciences, Institute of Geochemistry, Chinese Academy of Sciences, Guiyang (Guizhou), PR China
e-mail: liyang@mail.gyig.ac.cn
[3] Shandong Key Laboratory of Optical Astronomy and Solar-Terrestrial Environment, School of Space Science and Physics, Institute of Space Sciences, Shandong University, Weihai (Shandong), PR China
[4] Institute of Resources & Environment, Henan Polytechnic University, Jiaozuo (Henan), PR China
[5] Key Laboratory of Earth and Planetary Physics, Institute of Geology and Geophysics, Chinese Academy of Sciences, Beijing, PR China
[6] CNSA Macau Center for Space Exploration and Science, Macao, PR China
[7] Center for Excellence in Comparative Planetology, Chinese Academy of Sciences, Hefei (Anhui), PR China

Received 13 October 2022 / Accepted 19 December 2022

ABSTRACT

Context. E-type asteroids have been linked to aubrites, while M-type asteroids have been linked to enstatite chondrites (ECs) and iron meteorites (IMs). However, as ECs and IMs generally lack absorption characteristics, distinguishing their parent bodies by spectroscopy generally poses a challenge.
Aims. We aim to develop a method to distinguish two kinds of M-type asteroids, the parent bodies of ECs and IMs, and to infer their composition.
Methods. We measured the visible to near-infrared (VIS-NIR) reflectance spectra of aubrite, ECs, and IMs. Then we analyzed and compared their spectral parameters, such as the reflectance at 0.55 μm ($R_{0.55}$), absorption bands, and spectral slopes. We also compared the geometric albedo and spectral slopes of a total of 13 E-type and 14 M-type asteroids. Furthermore, combining the collected radar albedo and density data of M-type asteroids, we discuss their potential composition at different depths.
Results. We find that for most meteorites, with the exception of very weak absorption in an aubrite and an EH7 chondrite, ECs and IMs do not show any absorption characteristics. Aubrite shows extremely high reflectance and a negative near-infrared slope (NIRS) and ECs show relatively low reflectance and moderately positive NIRS, while IMs show relatively moderate reflectance and the steepest positive NIRS. Two diagrams plotting with $R_{0.55}$ and NIRS calculated in the 1.1–1.2 μm and 1.1–1.4 μm bands were subsequently shown to perform optimally at distinguishing aubrite, ECs, and IMs. In addition, M-type asteroids have a wide range of NIRS and diverse radar albedo and densities, whereby 16 Psyche shows high NIRS, radar albedo, and density, while 21 Lutetia is dominated by low values for these parameters.
Conclusions. We demonstrate that NIRS is correlated with metal content and increases with metal content. In particular, the NIRS calculated in the 1.1–1.4 μm band is a potentially useful parameter for inferring the surface metal content of E- and M-type asteroids. Based on our results, we suggest that the featureless M-type asteroids ought to be divided into two subtypes: Mm- (e.g., 16 Psyche) and Me-type (e.g., 21 Lutetia) in the aim of characterizing the sources of IMs and ECs, respectively.

Key words. minor planets, asteroids: general – meteorites, meteors, meteoroids – methods: analytical

1. Introduction

Main-belt asteroids and near-Earth asteroids are crucial for testing and modifying formation and evolution models of the Solar System. In particular, X-class asteroids (Tholen 1984) are of major importance because they represent about 20% part of inner main-belt objects and have the potential to host reduced bodies (Bell et al. 1989; Gradie & Tedesco 1982). Spectroscopically, X-class asteroids generally do not show obvious absorption features and they are composed of three types: E-, M-, and P- (Tholen 1984). In Tholen taxonomy, the E-, M-, and P-types are spectrally degenerate and defined based on the geometric albedo data: among them, the E-type represented bodies with the highest values (>0.3), while the M-type was determined as bodies with moderate values (0.1–0.3) and P-type displays the lowest values (Tholen 1984).

E-type asteroids are dynamically located in two areas: the Hungaria region from 1.88 to 1.98 AU and the inner main belt from 2.10 to 2.72 AU (Clark et al. 2004b). Based on spectral comparisons, E-type asteroids have been thought to be the parent bodies of aubrites (Zellner et al. 1977; Cloutis et al. 1990; Gaffey et al. 1992; Fornasier & Lazzarin 2001; Fornasier et al. 2008a). Aubrites are highly reduced achondrites that are formed in an environment with temperatures higher than 1000°C (McCoy et al. 1999). Mineralogically, aubrites are mainly composed of a high proportion (75–98 vol%) of iron-poor or iron-free enstatite ($En_{98.76–99.54}$), 0.3–10 vol% forsterite ($Fo_{99.79–99.99}$), 0.2–8.1 vol% diopside, <0.1–3.7 vol% metallic

FeNi, and <0.1–7.1 vol% troilite, along with trace amounts of minerals that imply highly reduced and anhydrous conditions: oldhamite, daubréelite, alabandite, and so on (Watters & Prinz 1979). E-type asteroids hence represent igneous bodies formed in a reduced anhydrous environment close to the Sun (Keil 1989). In particular, the Rosetta probe has performed the first flyby exploration mission for E-type asteroid 2867 Steins in 2008 (Keller et al. 2010), together with ground-based observation studies (Barucci et al. 2005; Nedelcu et al. 2007; Fornasier et al. 2008b), confirming that 2867 Steins is a typical parent body of aubrites and that the surface is dominated by reduced minerals such as enstatite and oldhamite. However, the best spectral-fitting model for 2867 Steins requires a 42% oldhamite (Nedelcu et al. 2007), which is far higher than the abundance found in aubrites (<0.1%; Watters & Prinz 1979; Keil 2010). In addition, with the improvement of observation accuracy, some E-type asteroids previously thought to be featureless do indeed show weak absorption characteristics. Therefore, E-type bodies have been classed into three subtypes by Gaffey & Kelley (2004): E[I] (featureless), E[II] (has 0.49 μm absorption, such as 2867 Steins), and E[III] (has 0.9 μm absorption), implying that various compositions may exist on their surfaces that impede a final determination of the nature of E-type asteroids. Most recently, the first sample return mission for E-type asteroid 10302 (1989 ML) was proposed by Lin et al. (2020), which is expected to bring definitive answers to questions on the composition and evolution of E-type asteroids.

Because of the similarities in their reflectance spectra (Clark et al. 2004a), M-type asteroids have been thought to be the source of iron meteorites (IMs; Gaffey & McCord 1979; Bell et al. 1989) and enstatite chondrites (ECs; Chapman & Salisbury 1973; Gaffey & McCord 1979). As the core fragments of differentiated and subsequently disrupted planetesimals (i.e., magmatic groups) or products crystallized in silicate molten pools (i.e., non-magmatic groups), IMs probably formed in the terrestrial planet region (Bottke et al. 2006) or the outer Solar System (Scott 2020). As the most reduced chondrites, ECs are composed of 50.6–74 vol% iron-poor enstatite ($En_{81.9–99.7}$), 5.0–15.8 vol% plagioclase, 0.2–1.1 vol% forsterite ($Fo_{99.2–99.6}$), 0.8–15.4 vol% metallic FeNi, 1.4–8.0 vol% troilite, and trace amounts of oldhamite (Kimura & Lin 1999), implying that they may have derived from undifferentiated planetesimals formed in the inner Solar System (Lin 2022). This is to say that although two M-types – parent bodies of IMs and parent bodies of ECs – show similar spectra, they have differences in their composition, origins, and evolution histories. Thus, distinguishing among them will allow for more accurate mappings of the distribution of materials in the Solar System (Gradie & Tedesco 1982; DeMeo & Carry 2014). In addition, understanding the composition of M-type asteroids will benefit the design of exploratory missions, such as Psyche (Reddy et al. 2019).

In order to clarify the composition of M-types, detailed spectroscopic observations have been performed, revealing variations in the absorption and spectral slopes (Rivkin et al. 1995, 2000; Clark et al. 2004a; Hardersen et al. 2005, 2011; Fornasier et al. 2010; Landsman et al. 2015; Takir et al. 2016) – rather than showing them to be featureless, as previously believed. Some of absorption characteristics of the M-type, such as 0.9 μm and 3 μm, may be contributed by external materials brought by impact processes of silicate-rich or hydrate-rich objects (Libourel et al. 2019). Since metal is more highly reflective of radar waves than silicate, the radar albedo can be used to roughly distinguish between metallic and nonmetallic bodies (Ostro et al. 1991; Virkki et al. 2014); for example, observations have shown that M-type asteroids possess a higher mean radar albedo than S- and C-type (Magri et al. 2001, 2007; Virkki et al. 2014). However, M-type asteroids have a wider range of radar albedo than others (Magri et al. 2007; Shepard et al. 2008, 2010, 2015), indicating the existence of both metal-rich and metal-poor objects. These make the composition of the M-type puzzling.

Comprehensive analyses of spectroscopic and radar observations promote the understanding of the composition of M-type asteroids (Ockert-Bell et al. 2008, 2010; Neeley et al. 2014). Ockert-Bell et al. (2008) noted that M-type asteroids with a steeper spectral slope (from 1.7 to 2.45 μm) tend to display higher radar albedo, which may indicate a metallic composition. Recently, a polarimetric observation work aimed at distinguishing iron-rich and iron-poor M-type asteroids was reported by Belskaya et al. (2022), which suggested that the depth of the negative polarization branch tends to increase with the near-infrared slope decreases. These points recall how valuable it could be to investigate the relationship between spectral parameters and mineralogy, especially with regard to the relationship between spectral slope and metallicity.

Considering that aubrites, ECs, and IMs represent the three different natural mineralogy: almost pure enstatite, enstatite-metal mixture, and almost pure metal, in this study, we focus on comparing their spectral parameters, aiming to investigate the sensitivity of reflectance spectra to the proportion of metal (or enstatite). We hope to find a useful spectroscopic method to distinguish aubrites, ECs, and IMs. Meanwhile, we expect the method applied to meteorites would also prove effective in distinguishing their parent asteroids.

Therefore, in the laboratory, we measured the visible to near-infrared (VIS-NIR) reflectance spectra of nine meteorites within the 0.35 to 2.5 μm wavelength, including aubrite, ECs, and IMs. Then, their spectral parameters, such as reflectance, absorption centers, band depth, and spectral slopes were calculated and compared in detail. We also calculated and compared the spectral parameters of thirteen E-type and fourteen M-type asteroids. Furthermore, in combining the data on reflectance spectra, radar albedo, and densities, we analyzed the potential compositions of these asteroids.

2. Samples and methods

2.1. Sample descriptions and processing

All the meteorite samples used in this study are listed in Table 1. Before performing the spectral measurements, all samples were kept in a dry chamber at room temperature (~25 °C) to avoid terrestrial contamination. Norton County is a fresh fragment, Huoyanshan is a block meteorite that resembles a fist, Gebel Kamil is a small block meteorite, and other samples are slabs. More detailed information on the samples is given in Appendix A.

Except for Norton County, both ECs and IMs were first ground by corundum (Al_2O_3) abrasives to expose a fresh area inside, then polished by a diamond polish agent with a size of 5 μm. This step ensures the freshness and flatness of the surface. Finally, the surfaces of all three IMs show gray color with no significant change in brightness with observation geometry, indicating a diffuse reflection, rather than a specular reflection surface. Since Norton County has a natural fracture surface, we did not grind and polish it.

2.2. Spectral measurements

Spectral data were obtained by the ASD FieldSpec 4 Hi-Res spectrometer installed at the Reflectance Spectroscopy

Table 1. Spectral parameters of 9 meteorites used in this study.

Type	Name	Observed fall	$R_{0.55}$	VISS		NIRS			
				$\mathbf{S}_1$	S_2	S_3	S_4	S_5	S_6
Aubrite	Norton county	Yes	0.51935	0.71028	0.34666	−0.09781	−0.04267	−0.06034	−0.08283
EH7	Itqiy	No	0.06299	−0.10851	0.11108	−0.24290	−0.01861	−0.00675	−0.01029
EH3	Qingzhen (enstatite)	Yes	0.10885	0.85483	0.66505	−0.01263	−0.00140	−0.01089	0.00288
EH3	Qingzhen (metal)	Yes	0.19019	1.17613	0.93653	0.32009	0.22487	0.15228	0.26922
EH4	Abee	Yes	0.07287	1.33680	1.59278	0.24566	0.16692	0.14108	0.10172
EH4	Indarch	Yes	0.06140	1.73752	3.10981	0.74750	0.17947	0.17214	0.06947
EL6	NWA 4945	No	0.07194	0.86373	0.75286	−0.01829	−0.00389	−0.00289	0.00325
IAB	Huoyanshan	No	0.15351	1.18791	0.78857	0.77450	0.62209	0.55861	0.44357
IIIAB	Dahongliuxia	No	0.14098	1.05728	0.47952	0.61094	0.41308	0.35914	0.15436
IM-ung	Gebel Kamil	No	0.07976	1.02075	0.59517	0.63073	0.41593	0.37850	0.21467

Notes. $R_{0.55}$ is absolute reflectance at 0.55 μm. S_1 to S_6 are spectral slopes calculated within 0.4–0.5 μm, 0.5–0.6 μm, 0.8–0.9 μm, 1.1–1.2 μm, 1.1–1.4 μm, and 1.6–1.8 μm bands, respectively. The Qingzhen (enstatite) refers to the area richer in enstatite in Qingzhen meteorite, while Qingzhen (metal) refers to the area richer in metal in Qingzhen meteorite. -ung means the meteorite is ungrouped.

Laboratory of Shandong University in Weihai, Shandong Province, China. This spectrometer is equipped with a 512-element silicon array detector (0.35–1.0 μm) and two Graded Index InGaAs detectors (1.001–1.8 μm, and 1.801–2.5 μm) to collect VIS-NIR reflectance spectral signals from 0.35 to 2.5 μm wavelength. Its light source is an ASD illuminator with a 57 W quartz-tungsten-halogen lamp, which can provide stable illumination over a 0.35–2.5 μm range for spectral measurement. The spectral resolution is 3 nm at 0.7 μm, and 8 nm at 1.4 μm and at 2.1 μm. The spectral sampling is 1.4 nm in the 0.35–1.0 μm region and 1.1 nm in the 1.001–2.5 μm region. Before measuring the spectra of samples, we first used a Spectralon Diffuse Reflectance Standard white plate for calibration and then set up the relative positions of the light source, white plate, and optical fiber probe as follows: (1) adjusting the position of the light source so that the light source is 30 cm away from the surface of standards, forming a uniform illumination spot with a diameter of approximately 6.3 cm; (2) adjusting the position of the detection fiber so that it is 5 mm from the surface of the white plate to ensure that all of the collected signals come from a circular area with a diameter of ∼3 mm; (3) measuring the spectrum of each sample in turn.

For each sample spot, the spectral signal was repeatedly collected 300 times and the average value was taken. The dark current was collected 100 times and averaged at each sample spot, then it was subtracted from the measurement. All the spectral measurements were performed with a phase angle of 30° (incident angle is 0°, and emission angle is 30°) in the air environment and the thermal radiation from the light source caused the surface temperature of samples to reach ∼40 °C.

As for the spectral measured area, Norton County was chosen for its natural fracture surface. Two areas of the Qingzhen meteorite were measured, respectively, with one being relatively more metal-rich and marked as Qingzhen (metal), and the other more enstatite-rich and marked as Qingzhen (enstatite). The other meteorites were all measured in their fresh areas with homogeneous composition to maximize the reflection of comprehensive spectral information.

2.3. Spectral analysis

For each meteorite sample, we investigated their visible reflectance at 0.55 μm ($R_{0.55}$), absorption center (AC), band depth (BD), and spectral slopes calculated in different bands (S_n). We used the software ENVI (5.3.1 version) to calculate the absorption center and band depth: (1) importing the spectral data (extension is .txt) using the "Display–Spectral Library Viewer–Import–ASCII" option; (2) removing the continuum using the "Continuum Removed" option, which uses the algorithm described in Clark & Roush (1984); (3) noting that in the absorption bands, the wavelength corresponding to the lowest value of the vertical axis is the absorption center and the band depth is the value that 1 minus the lowest value of the vertical axis in the absorption bands.

Utilizing the linear fitting method (the fitting tool is provided with software OriginPro 2021) for spectral curves that were normalized at 0.55 μm, we calculated the visible slope (VISS) in two bands (0.4–0.5 μm and 0.5–0.6 μm) and the near-infrared slope (NIRS) in four bands (0.8–0.9 μm, 1.1–1.2 μm, 1.1–1.4 μm, and 1.6–1.8 μm). S_1 to S_6 sequentially symbolize the spectral slopes calculated in 0.4–0.5 μm, 0.5–0.6 μm, 0.8–0.9 μm, 1.1–1.2 μm, 1.1–1.4 μm, and 1.6–1.8 μm bands. In Appendix B, we elaborate on the reasons we chose these bands. In addition, we provide a sketch Fig. B.1 to visually illustrate these spectral parameters. Table 1 lists the calculated parameters of all the meteorites in detail.

For the spectra of asteroids, as most of them have been processed by normalization at a certain wavelength (e.g., 0.55 μm or 1.215 μm), removing the value of absolute reflectance, we thus adopted the geometric albedo (Pv) to reflect their brightness. As in the case of meteorites, using the liner fitting tool, we also calculated the spectral slopes in different bands. In contrast to our approach to meteorites, and due to the lack of some spectral data in the shortwave region, we did not calculate the slope in the 0.4–0.5 μm band for asteroids. In addition, for convenience in terms of distinguishing asteroids from meteorites, we adopted the "SSn" to represent the slopes of asteroids, and SS_2 to SS_6 sequentially refers to slopes calculated in the 0.5–0.6 μm, 0.8–0.9 μm, 1.1–1.2 μm, 1.1–1.4 μm, and 1.6–1.8 μm bands. Tables 2 and 3 list the spectral parameters of these asteroids.

3. Results

3.1. Spectra of meteorites

Figure 1 shows the reflectance spectra of meteorites measured in this study. In the whole VIS–NIR region, aubrite Norton County presents the highest reflectance, while ECs and IMs

Table 2. Spectral parameters of 13 Tholen E-type asteroids.

Number	Name	Pv	VISS	NIRS				Spectrum file
			SS_2	SS_3	SS_4	SS_5	SS_6	
44	Nysa	0.55[a]	0.26071	−0.30213	0.08491	0.10482	−0.00994	data18/44_00.tab[aa] clarketal2004/44_010621t124137.tab[bb]
64	Angelina	0.43[a]	1.56031	−0.01417	0.10168	0.09178	0.02124	data24/64_00.tab[aa] clarketal2004/64_001008t150913.tab[bb]
214	Aschera	0.52[a]	0.87757	−0.37757	0.11242	0.00313	−0.04650	data08/214_01.tab[aa] clarketal2004/214_030816t055017.tab[bb]
317	Roxane	0.49[a]	0.40649	−0.36546	0.2132	0.0234	−0.07508	data13/317_01.tab[aa] clarketal2004/317_010315t134132.tab[bb]
434	Hungaria	0.46[a]	1.67982	−0.35246	0.15821	0.15015	0.02921	data18/434_01.tab[aa] clarketal2004/434_010823t121908.tab[bb]
504	Cora	0.34[a]	0.1628	−0.05675	0.18001	0.1254	0.13082	data20/504_01.tab[aa] hardersen_et_al_2011/cora1.tab[cc]
1103	Sequoia	0.48[a]	0.65221	−0.16817	0.18278	0.09427	0.01577	data01/1103_01.tab[aa] clarketal2004/1103_030816t072356.tab[bb]
1251	Hedera	0.41[a]	0.27513	−0.29621	0.26483	0.12704	0.06806	data02/1251_01.tab[aa] clarketal2004/1251_030818t132430.tab[bb]
2035	Stearn	0.649[b]	1.23277	−0.14563	0.20269	0.18693	0.09540	data07/2035_00.tab[aa] 2002/2035_stearns.tab[dd]
2867	Seteins	0.45[c]	No data	No data	0.09384	0.04162	0.01596	a002867.sp58[ee]
3103	Eger	0.63[d]	1.85509	0.13952	0.30242	0.18568	0.0472	a003103.sp06[ee]
4660	Nereus	0.55[b]	0.52886	0.25313	0.30141	No data	−0.11529	a004660.6[ff]
10302	1989 ML	0.37[e]	0.40559	−0.47286	0.12934	0.0145	0.04228	a010302.4[gg] a010302.sp112p2[ee]

Notes. Pv is geometric albedo. SS_2 to SS_6 are spectral slopes calculated within 0.5–0.6 μm, 0.8–0.9 μm, 1.1–1.2 μm, 1.1–1.4 μm, and 1.6–1.8 μm bands, respectively. Pv are collected from [a]Tedesco et al. (2002), [b]JPL Small-Body Database Browser web (https://ssd.jpl.nasa.gov/sbdb.cgi), [c]Fornasier et al. (2006), [d]Veeder et al. (1989), and [e]Mueller et al. (2007). Spectral files are collected from [aa,bb,cc,dd]Small Bodies Data Ferret web (https://sbnapps.psi.edu/ferret/SimpleSearch/results.action) and [ee,ff,gg]MIT web (http://smass.mit.edu/catalog.php). The detailed information about spectral files please see [aa]Bus & Binzel (2002), [bb]Clark et al. (2004b), [cc]Hardersen et al. (2011), [ee]Rayner et al. (2003), [ff]Binzel et al. (2004), and [gg]Binzel et al. (2001).

Table 3. Spectral parameters of 14 Tholen M-type asteroids.

Number	Name	Pv	VISS	NIRS				Spectrum file
			SS_2	SS_3	SS_4	SS_5	SS_6	
16	Psyche	0.15[a]	0.23087	0.26395	0.18992	0.46238	0.47042	compspectra/16psyche.tab[aa]
21	Lutetia	0.22[b]	0.28363	0.16876	0.16618	0.12613	−0.00198	a000021.sp31[bb]
22	Kalliope	0.14[b]	0.30581	0.19390	0.36398	0.29601	0.13907	compspectra/22kalliope.tab[aa]
97	Klotho	0.23[b]	0.47667	0.20579	0.20207	0.14219	−0.01086	compspectra/97klotho.tab[aa]
110	Lydia	0.2[c]	0.35034	0.32301	0.41032	0.31249	0.20262	compspectra/110lydia.tab[aa]
135	Hertha	0.14[b]	0.80381	0.10787	0.27165	0.20695	0.08151	compspectra/135hertha.tab[aa]
161	Athor	0.22[c]	0.28389	−0.46231	0.09934	0.23059	0.09703	compspectra/161athor.tab[aa]
201	Penelope	0.12[c]	0.34204	−0.21946	0.21012	0.18491	0.13397	a000201.sp28[bb]
216	Kleopatra	0.12[b]	0.52189	0.11672	0.32356	0.24372	0.11776	data08/216_01.tab[cc] clarketal2004/216_020617t065422.tab[dd]
224	Oceana	0.17[b]	0.57469	0.33347	0.51499	0.29717	0.13566	acompspectra/224oceana.tab[aa]
325	Heidelberga	0.11[b]	No data	0.47282	0.39964	0.33339	0.24769	hardersen_et_al_2011/heidelberga.tab[ee]
347	Pariana	0.18[b]	No data	−0.15624	0.25736	0.14411	0.20333	hardersen_et_al_2011/pariana.tab[ee]
441	Bathilde	0.14[b]	0.81839	0.42681	0.20652	0.30583	0.19853	compspectra/441bathilde.tab[aa]
872	Holda	0.21[b]	0.36993	0.03151	0.43481	0.32747	0.12351	compspectra/872holda.tab[aa]

Notes. Pv are collected from [a]Shepard et al. (2017), [b]Tedesco et al. (2002), and [c]Shepard et al. (2015). Spectral files are collected from [aa,cc,dd,ee]Small Bodies Data Ferret web (https://sbnapps.psi.edu/ferret/SimpleSearch/results.action) and [bb]MIT web (http://smass.mit.edu/catalog.php). The detailed information about spectral files please see [aa]Fornasier et al. (2010), [bb]Rayner et al. (2003), [cc]DeMeo et al. (2009), [dd]Clark et al. (2004a), and [ee]Hardersen et al. (2011).

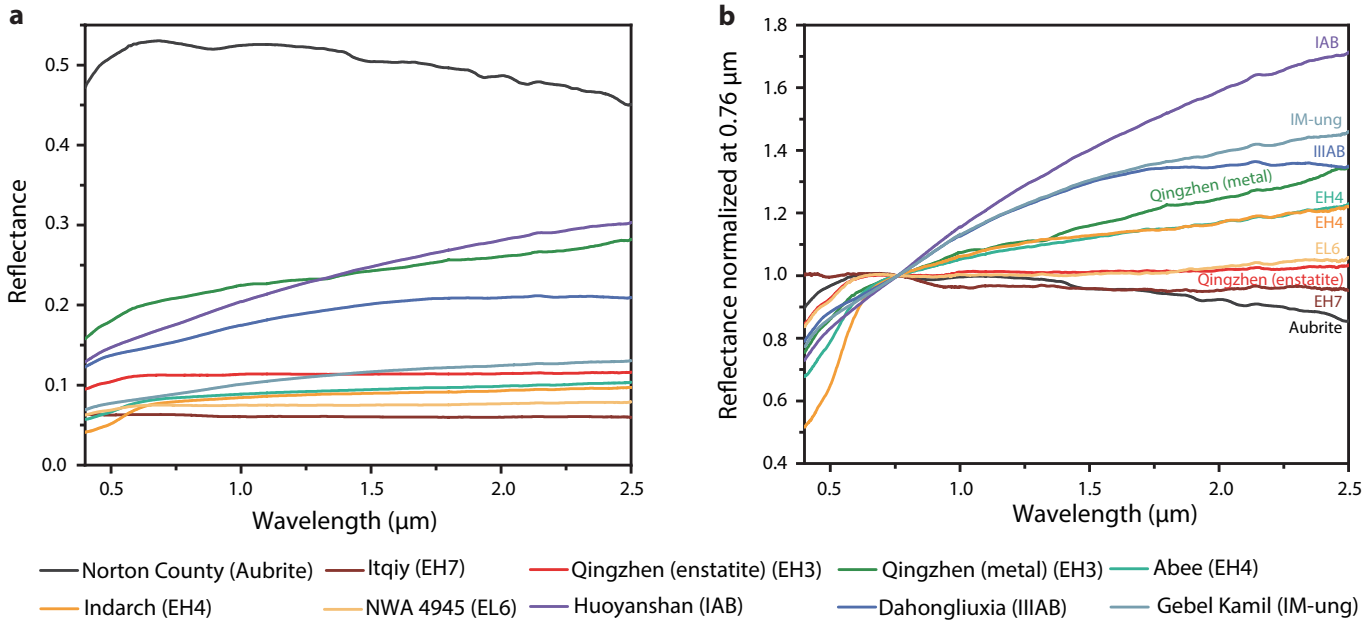

Fig. 1. Reflectance spectra of nine meteorites: (*a*) Reflectance changes with wavelength. (*b*) Reflectance normalized at 0.76 μm changes with wavelength. In (*b*), the iron meteorites show the steepest near-infrared slope, enstatite chondrites show the moderate near-infrared slope, and aubrite shows the lowest near-infrared slope, indicating that the near-infrared slope is related to the proportion of metal (or enstatite) in the enstatite-metal mixed system.

show moderate reflectance (Fig. 1a). Figure 1b suggests that in the near-infrared region (0.76–2.5 μm), IMs show the steepest positive slope, and the near-infrared curve of Qingzhen (metal) is flatter than IMs but steeper than ECs and Qingzhen (enstatite). For ECs, two EH4 meteorites (Abee and Indarch) show the steepest positive slope, EL6 NWA 4945 shows the flat curve, while EH7 Itqiy shows a weakly negative slope (Fig. 1b). Compared with IMs and ECs, aubrite Norton County presents the most relatively steep negative slope. This seems to suggest that reflectance and the near-infrared slope are related to types of meteorites. The detailed analysis of spectral parameters is described in Sects. 3.1.1–3.1.3.

3.1.1. Absorption center (AC) and band depth (BD)

Here, we identify three weak absorption bands in aubrite Norton County, namely: 0.892 μm (BD is 1.8%), the signal of enstatite containing a trace amount of ferrous iron (Fe^{2+}), 1.49 μm (BD is 1.53%) and 1.937 μm (BD is 1.28%), two signals of hydroxyl (-OH), and adsorbed water (H_2O; Table 4). For ECs, only EH7 Itqiy shows four very weak absorption at 0.494 μm (BD is 1.21%), 1.035 μm (BD is 2.65%), 1.802 μm (BD is 1.86%), and 1.937 μm (BD is 1.89%). Here, 0.494 μm belongs to the signal of oldhamite, 1.035 μm and 1.802 μm indicate enstatite or forsterite containing a trace amount of Fe^{2+} (Table 4). The presence of 1.49 μm and 1.937 μm in Norton County, and 1.937 μm in Itqiy, may be caused by terrestrial weathering. In addition, Norton County and Ityiy show weak absorption at 2.102 μm and 2.2 μm, respectively, which is similar to the signal of Al–OH or Fe–OH in phyllosilicates (products of aqueous alteration of olivine or pyroxene), as shown in Table 4, may also imply the terrestrial weathering. The weathered Norton County sample measured by Penttilä et al. (2018) also shows the signal of –OH or H_2O. The weak 1.4 μm, 1.9 μm, and 2.2 μm even deep 3 μm bands were also seen in synthetic enstatites (Markus et al. 2018). This specifically reminds us that enstatite is very susceptible to being weathered in the air environment and meteorites richer in enstatite should be kept in a dry-vacuum environment instead of the atmosphere.

However, we also see the weak 2.2 μm absorption (BD <1%) in all remaining ECs and IMs. Considering that (1) except for the 2.2 μm feature, the remaining ECs and IMs did not show any absorption of -OH or H_2O across the VIS-NIR region; (2) it seems difficult to produce the phyllosilicates by aqueous alteration of IMs; (3) the Spectralon standard plate has a small positive peak at 2.1 μm and absorption at 2.15–2.2 μm (Zhang et al. 2014), similarly to our results; hence, we tend to believe that the 2.2 μm features in our samples are pseudo-absorption caused by Spectralon standard plate. Of course, since Norton County and Itqiy also show absorption of –OH or H_2O at other positions, their 2.1–2.2 μm features may be contributed by a combination of terrestrial weathering effect and signal of Spectralon standard plate. In summary, the weak absorption features in the enstatite-rich system are worth continuing study in the future, as various weak absorption have been noticed in E- and M-type asteroids. Here, our samples show that EH7 Itqiy seems to be more similar to aubrite in terms of absorption characteristics rather than ECs.

3.1.2. Reflectance at 0.55 μm ($R_{0.55}$)

As shown in Fig. 1 and Table 1, aubrite Norton County shows the highest reflectance across the whole VIS–NIR region, particularly the value of $R_{0.55}$ is more than 0.5, significantly higher than other meteorites. ECs and IMs all show relatively lower but very close reflectance ($R_{0.55}$ fall into the range of 0.06140–0.10885 and 0.07976–0.19019, respectively), exhibiting some degree of overlap.

3.1.3. Spectral slope (S_n)

In Fig. 1, the spectral curve of aubrite Norton County shows an upward trend in the visible region but a downward trend in the

Table 4. Reasons for absorption in meteorites.

AC (μm)	Reasons	Reference
0.44–0.51	Oldhamite	Burbine et al. (2001)
0.88–0.9	Trace amount of Fe^{2+} in enstatite pyroxene	Gaffey & Kelley (2004)
1	Electronic transitions of Fe^{2+} in olivine and crystal field transitions of Fe^{2+} in pyroxene	Burns (1970); Clark Jr (1957)
1.4	First overtone of hydroxyl (–OH) stretches	Clark et al. (1990)
1.8	Trace amount of Fe^{2+} in enstatite pyroxene	Gaffey & Kelley (2004)
1.93–1.94	Adsorbed water (H_2O)	Aines & Rossman (1984); Cloutis (1989)
2	Crystal field transitions of Fe^{2+} in pyroxene	Burns (1970); Clark Jr (1957)
2.2–2.3	Metal-OH bends in phyllosilicates	Clark et al. (1990)

near-infrared region, which could also be seen in Table 1, where S_1 and S_2 have positive values, while S_3 to S_6 are all negative, indicating a blue NIRS. EH7 Itqiy is similar to aubrite Norton County in curve shape (Fig. 1) but has the bluish NIRS (values of S_3 to S_6 are all slightly negative). EH3 Qingzhen (metal) shows obvious red NIRS, in which S_3 to S_6 are all positive, while EH3 Qingzhen (enstatite) is similar to EH7 Itqiy and displays bluish NIRS (S_3 to S_5 are all slightly negative). Similarly to EH3 Qingzhen (enstatite) and EH7 Itqiy, EL6 NWA4945 also has bluish NIRS (S_3 to S_5 are slightly negative). Similarly to EH3 Qingzhen (metal), EH4 Abee and Indarch show relatively steeper near-infrared curves and higher values of S_3 to S_6 than EH7 Itqiy, EH3 Qingzhen (enstatite), and EL6 NWA 4945. Three iron meteorites, Huoyanshan, Dahongliuxia, and Gebel Kamil, all have intensively red NIRS (S_3 to S_6 are all positive). To sum up, IMs show the steepest positive values of NIRS; EH3 Qingzhen (metal), EH4 Abee, and EH4 Indarch show moderate positive values of NIRS; EH3 Qingzhen (enstatite), EH7 Itqiy, and EL6 NWA 4945 have slightly negative values of NIRS; whereas aubrite Norton County has the obvious negative values of NIRS.

Considering the difference of composition among these meteorites that (1) aubrite Norton County is composed of the highest proportion of enstatite (84.5%) and the lowest proportion of metal (0.3% FeNi; Watters & Prinz 1979); (2) EH7 Itqiy and EL6 NWA4945 have a slightly lower enstatite proportion (74–78%) and higher metal content (8–22% kamacite) than aubrite Norton County (mineralogy data are collected from Meteoritical Bulletin Database[1]); (3) EH4 meteorites are composed of a mixture of enstatite and metal, showing a moderate enstatite and metal content (58.8–72.6% enstatite and 17.5–23.8% FeNi; Keil 1968); (4) IMs represent a more metal-rich member (proportion of FeNi is close to 100%) than EH4; (5) the difference in metal content between Qingzhen (metal) and Qingzhen (enstatite); and (6) the spectral measured results of S_3 to S_6 among these meteorites, it strongly indicates that the near-infrared slope of the meteorite is sensitive to the content of metal and enstatite. Wherein the metal controls the NIRS to turn red, while enstatite controls the NIRS to turn blue and NIRS increases as metal content increases while decreases as enstatite content increases. In two visible bands (0.4–0.5 μm and 0.5–0.6 μm), we did not find a systematic difference in slope among aubrite, IMs, and ECs. However, it is noteworthy that Norton County shows the steepest slope within the 0.4–0.5 μm band, which is affected by the ultraviolet band because enstatite tends to have a steep ultraviolet slope (Markus et al. 2018).

[1] https://www.lpi.usra.edu/meteor/

3.2. "$R_{0.55}$–NIRS" diagram for meteorite classification

From Sects. 3.1.1 to 3.1.3, we note three types of meteorites (aubrite, ECs, IMs) that have an almost independent range of $R_{0.55}$ and NIRS (S_3, S_4, S_5, S_6). In order to visually present this result, we plot $R_{0.55}$ with S_3, S_4, S_5, and S_6 in four diagrams, respectively (see Figs. 2c to f). For comparison, $R_{0.55}$ with S_1 and S_2 were also plotted, respectively, in Figs. 2a and b. In Figs. 2a and b, data points of different types of meteorites may appear confusing (i.e., it is difficult to distinguish different types of meteorites using $R_{0.55}$ and visible slopes). In Figs. 2c and f, although IMs show systematically higher spectral slopes, there is still a small overlap between ECs and IMs. In Figs. 2d and e, we see that aubrite, ECs, and IMs are completely isolated from each other. These results indicate that plotting with $R_{0.55}$ and NIRS is effective in identifying types of meteorites, working best when slopes are calculated in the 1.1–1.2 μm and 1.1–1.4 μm bands. In some sense, it provides a possibility for identifying aubrite, ECs, and IMs via spectroscopy, which would be particularly useful for distinguishing IMs and ECs. This highlights the fact that plotting with reflectance and NIRS may also be able to distinguish the parent asteroids of these meteorites. We check this assumption in Sect. 3.3.

3.3. "Pv–NIRS" diagram for E- and M-type asteroids classification

We collected the observed spectral data from representative thirteen E-type asteroids (see Table 2) and fourteen M-type asteroids (see Table 3), and analyzed their spectral parameters. Similarly to the meteorite processing method, we plotted the diagram using Pv and NIRS in turn (see Fig. 3).

Figure 3 suggests that asteroids have similar trends in brightness and spectral slope compared with meteorites. Among them, E-type asteroids show a higher geometric albedo ($Pv > 0.3$), while M-type asteroids show a lower geometric albedo. As for spectral slope, in 0.5–0.6 μm and 0.8–0.9 μm bands (Figs. 3a and 3b), the slope range of E-type overlaps with M-type at a high degree. However, in the 1.1–1.2 μm, 1.1–1.4 μm, and 1.6–1.8 μm bands (Figs. 3c–e), M-type asteroids show an overall higher slope than E-type. In particular, in the 1.1–1.4 μm band, the range of slopes for E-types overlaps with M-types the least, indicating that plotting with Pv and SS_5 could be best at distinguishing among these types. However, it is worth noting that (1) E-type asteroids almost all show positive NIRS while their daughter aubrite shows negative NIRS; (2) the slope range of E-type does not show a clear boundary with M-type. These two issues may be caused by the space weathering (SW) effects,

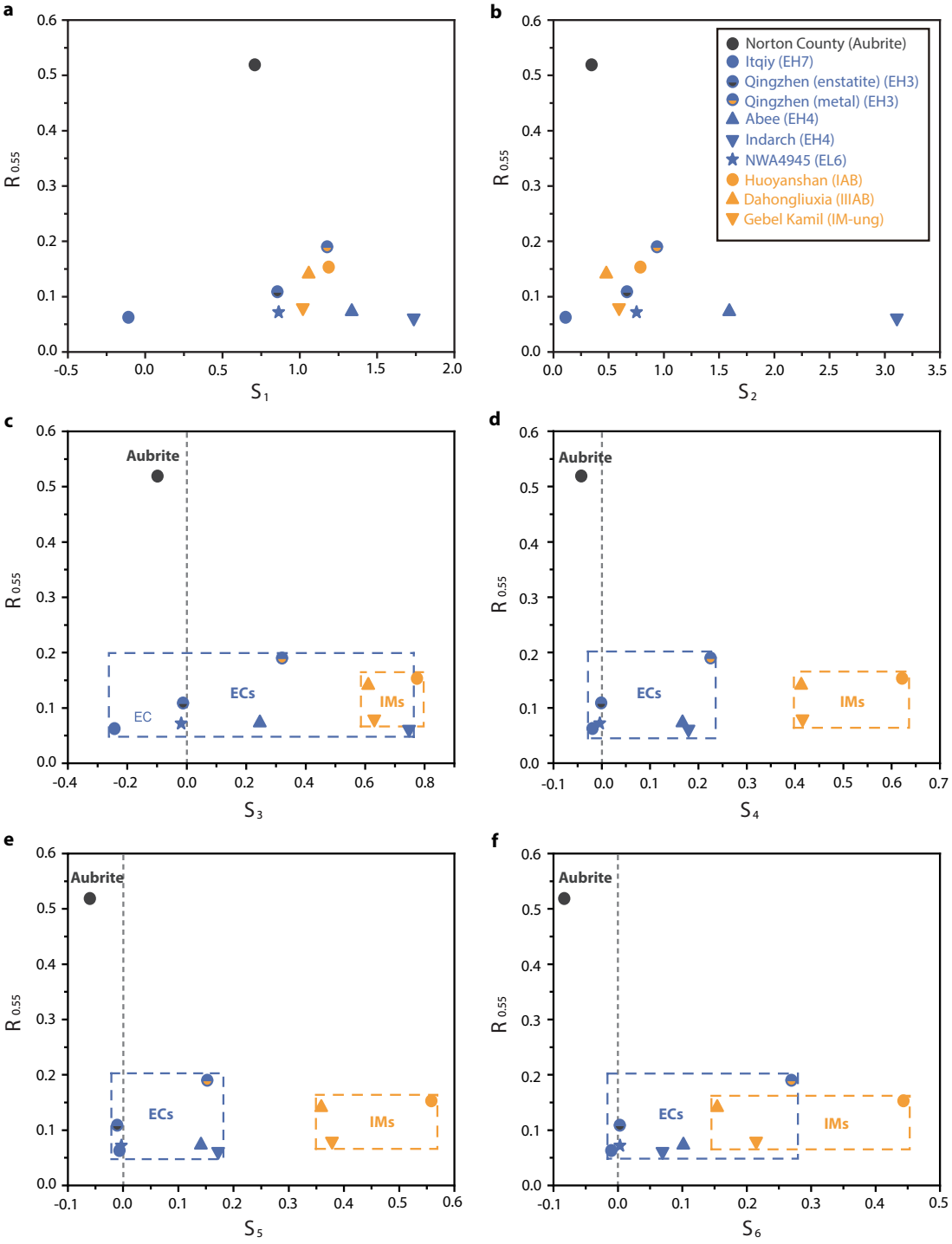

Fig. 2. For meteorites, the diagram plotted by reflectance at 0.55 μm ($R_{0.55}$) and spectral slope calculated in six short bands, respectively. S_1 to S_6 sequentially refer to the spectral slopes calculated in 0.4–0.5 μm, 0.5–0.6 μm, 0.8–0.9 μm, 1.1–1.2 μm, 1.1–1.4 μm, and 1.6–1.8 μm bands.

which is further discussed in Sect. 4.1. Of course, considering the complexity of asteroids, these two issues may also be caused by different composition or particle size effects of regolith. We also discuss these issues in the section below.

In addition, we noticed that M-type asteroids show a wide range of NIRS, in which 16 Psyche has the highest SS_5 (0.46238), while 21 Lutetia has the lowest SS_5 (0.12613), (Fig. 3d). According to the results of our measured meteorites above, it is possible that M-type asteroids with steeper NIRS have more metal-rich surfaces, while M-type asteroids with relatively flatter NIR curves have more enstatite-rich surfaces. In the following section, we provide a comprehensive analysis of spectroscopy, radar albedo, and density.

4. Analysis and discussion

4.1. Influence of SW for aubrite-ECs-IMs classification and E- and M-type asteroids classification

In Sect. 3.3, we mention that the difference in spectral slopes between meteorites and asteroids may be caused by the SW effects. Here, using pulsed lasers to irradiate aubrite Norton

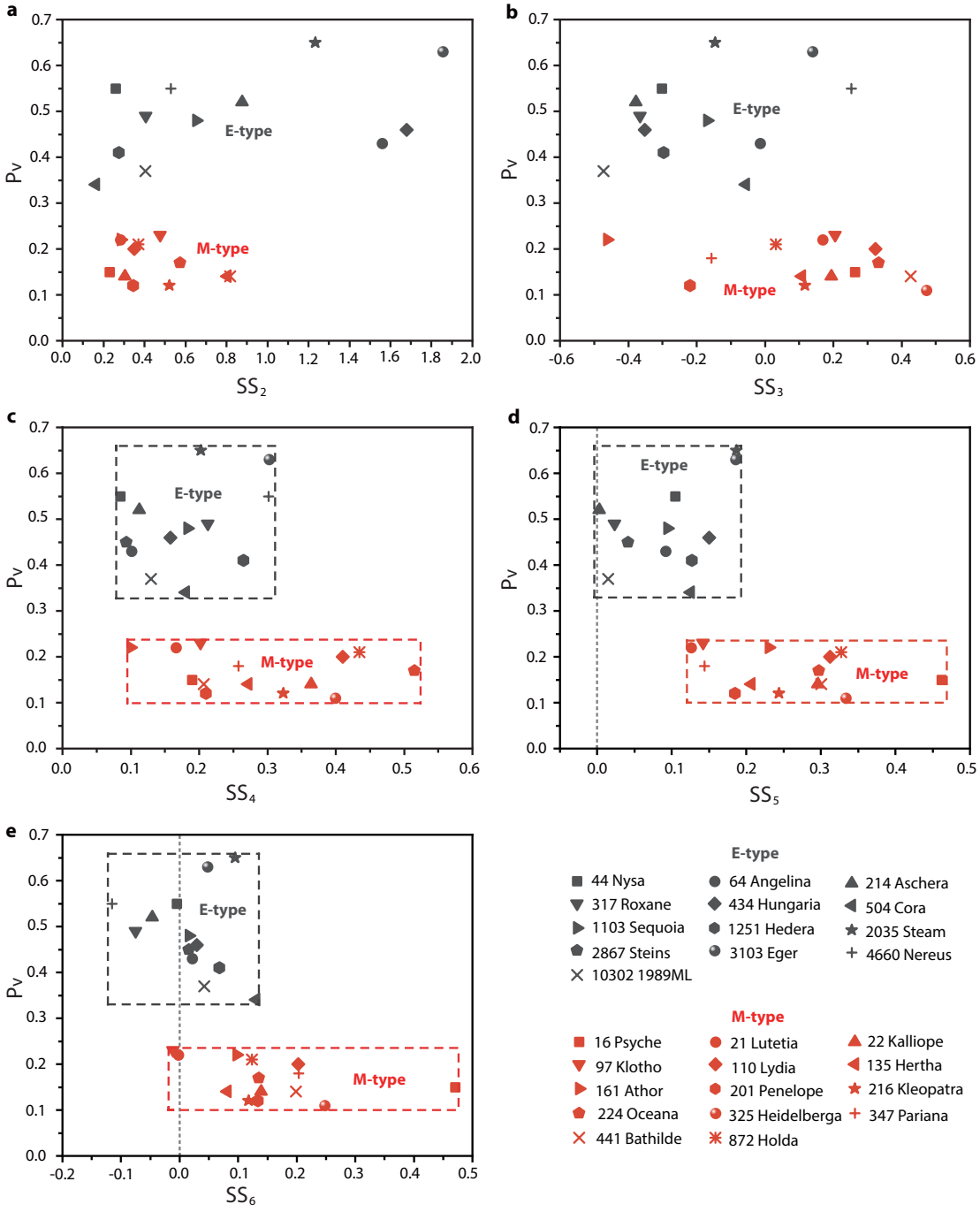

Fig. 3. For asteroids, the diagram plotted by geometric albedo (Pv) and spectral slope calculated in five short bands. SS_2 to SS_6 sequentially refer to the spectral slopes calculated in 0.5–0.6 μm, 0.8–0.9 μm, 1.1–1.2 μm, 1.1–1.4 μm, and 1.6–1.8 μm bands.

County, EH4 Abee, EH4 Indarch, and IIIAB Dahongliuxia in the laboratory – as laser irradiation of meteorites can simulate the SW process driven by micrometeoroid bombardments on asteroids (Sasaki et al. 2001) – we show how the SW effects affect the spectral slopes. In the vacuum chamber (5×10^{-6} mbar), each meteorite was irradiated 10 shots at the energy of 28 mJ per shot. We previously reported the detailed irradiated process, space weathering spectral alteration effects (SWSAE), along with a microanalysis for Norton County, Abee, and Indarch in Zhang et al. (2022). In this paper, we additionally release the spectral data of unirradiated and irradiated iron meteorite Dahongliuxia and carry out a micro-observation for irradiated Dahongliuxia.

Figure 4a shows the spectral curves of Norton County, Abee, Indarch, and Dahongliuxia before and after irradiation. Figure 4b shows their $R_{0.55}$ and S_5 values before and after irradiation.

As shown in Fig. 4a, after irradiation, for aubrite Norton County, reflectance decreases across the VIS-NIR region and curve steeps; for EH4 Abee and Indarch, reflectance increases across the VIS-NIR region and curve steeps; for IIIAB Dahongliuxia, VIS-NIR reflectance intensely increases while curve flattens. These changes can also be seen in Fig. 4b: here, $R_{0.55}$ of Norton County decreases from 0.51935 to 0.25141 and S_5 increases from –0.06034 to –0.00454; $R_{0.55}$ of Abee increases from 0.07287 to 0.08093 and S_5 increases from 0.14108

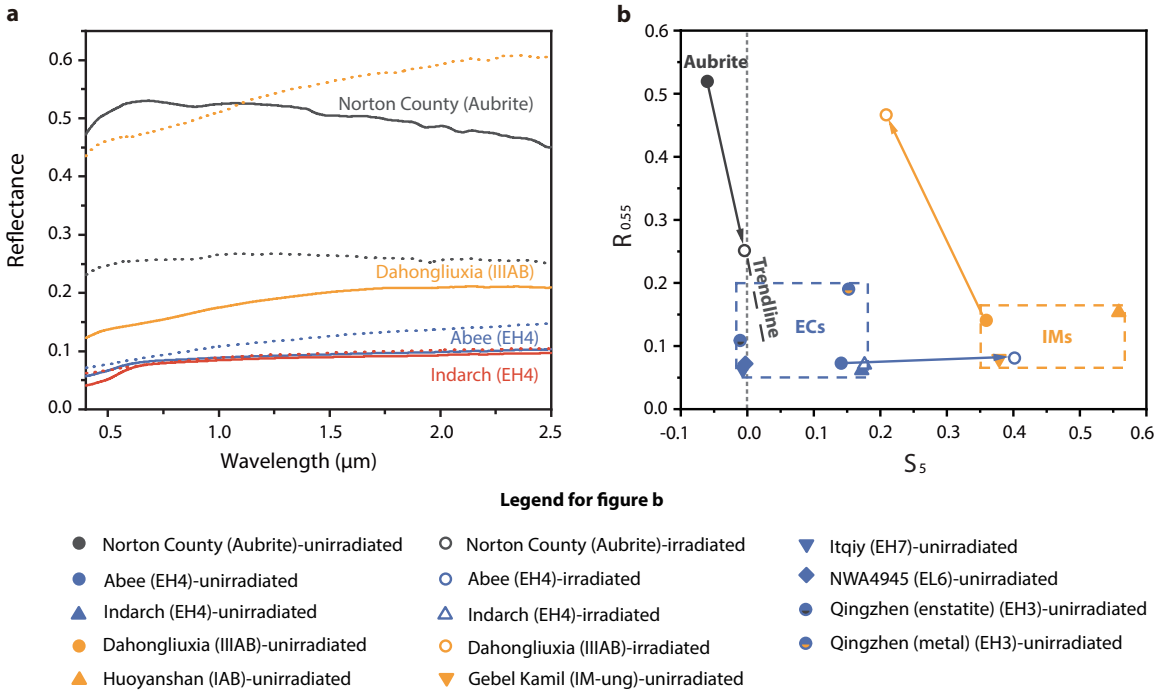

Fig. 4. Space weathering spectral alteration effects simulated by laser irradiating meteorites. (*a*) Reflectance changes with wavelength. The solid lines represent unirradiated spectra, and the dashed lines represent irradiated spectra. (*b*) The diagram plotted by reflectance at 0.55 μm ($R_{0.55}$) and the spectral slope calculated in the 1.1–1.4 μm band (S_5). The solid symbols represent unirradiated meteorites, and the open symbols represent irradiated meteorites. The arrows point from unirradiated to irradiated samples, reflecting the trend of data point migration caused by laser irradiation. We note that the dashed line marked "trendline" is a virtual extension line of the black arrow.

to 0.40167; $R_{0.55}$ of Indarch increases from 0.06140 to 0.07025 and S_5 increases from 0.17214 to 0.17630; $R_{0.55}$ of Dahongliuxia increases from 0.14098 to 0.46630 and S_5 decreases from 0.35914 to 0.20881. These results suggest that laser irradiation alters the original location of meteorites in Fig. 2e.

In Fig. 4b, we see that when the SW degree continues to increase, for aubrite Norton County, the value of S_5 is very likely to eventually turn positive, as for E-types. Meanwhile, the irradiated point of Norton County may move along the trendline and finally fall into the range of ECs (see Fig. 4b). This may indicate that some weathered parent bodies of aubrite may be easily recognized as unweathered (fresh) parent bodies of ECs, suggesting that SW may blur the spectral boundary between E- and M-type asteroids, leading to a partial overlap of NIRS range between E- and M-type asteroids.

Laser irradiation produces the thick amorphous rim (~350 nm) without nanophase metallic particles on Norton County (see Fig. 4c in Zhang et al. 2022). As with the Moon (McKay et al. 1991), amorphization could contribute to darkening and reddening spectral effects, possibly due to changes in optical constants of host minerals by amorphous rim. Considering the connection between aubrite and E-type asteroids, amorphization may also exist on the surfaces of E-type asteroids. In addition, since E-type bodies are generally closer to the Sun than other types (Gradie & Tedesco 1982; DeMeo & Carry 2014), they may have undergone higher speed micrometeoroid bombardments and greater flux of solar wind irradiation (another important SW process Pieters & Noble 2016). Hence, amorphization caused by SW may be the one of significantly important aspects of darkening and reddening the fresh E-type asteroid surfaces. Of course, we should not completely rule out the contributions that come from other SW products, such as nanophase iron (npFe^0) or submicroscopic iron, which may be produced due to the impact between iron-bearing impactors and E-type bodies and can play a similar role in spectral alteration as amorphization (Noble et al. 2007; Pieters & Noble 2016).

In addition to the SW effect, the particle size effect may also contribute to the spectral slope difference between our Norton County sample and E-type asteroids. Reddy et al. (2016) reported that chip of aubrite trend to show bluer NIRS (similar to our Norton County) than the powder sample, and NIRS increases with decreasing particle size. Considering that E-type asteroids generally have large diameters (Fornasier et al. 2008a) and may have developed fine-sized particles, such as S-type 433 Eros (Clark et al. 2001), the red slope of E-type asteroids shown in Figs. 3c to e may be also contributed by fine-sized regolith.

Because of the melting and sputtering of metal (which increase the proportion of metal on the surface; see Fig. 5 in Zhang et al. 2022), two EH4 meteorites, Abee and Indarch, both become brighter and redder after irradiation (see Fig. 4a); wherein the irradiated Abee even falls into the range of virgin (unirradiated) iron meteorites (see Fig. 4b). This indicates that SW is likely to confuse the spectroscopic boundaries between weathered parent bodies of ECs and unweathered parent objects of IMs.

Laser irradiation of Dahongliuxia has given a brighter and bluer SWSAE (Fig. 4). Microanalysis shows that laser irradiation of iron meteorites can lead to the melting and flowing of metal and produce fine-sized FeNi (see Wu et al. 2017 and Fig. 5b in this study). Although the fine-sized FeNi particles can contribute to the darker and redder spectra (Britt & Pieters 1994), after irradiation, the total surface roughness of Dahongliuxia may be reduced due to a large number of small smooth planes produced by the melting-flowing-cooling effect of the metal. Cloutis et al. (2010) noticed that for slab iron meteorites, reducing surface roughness can increase reflectance and reduce near-infrared

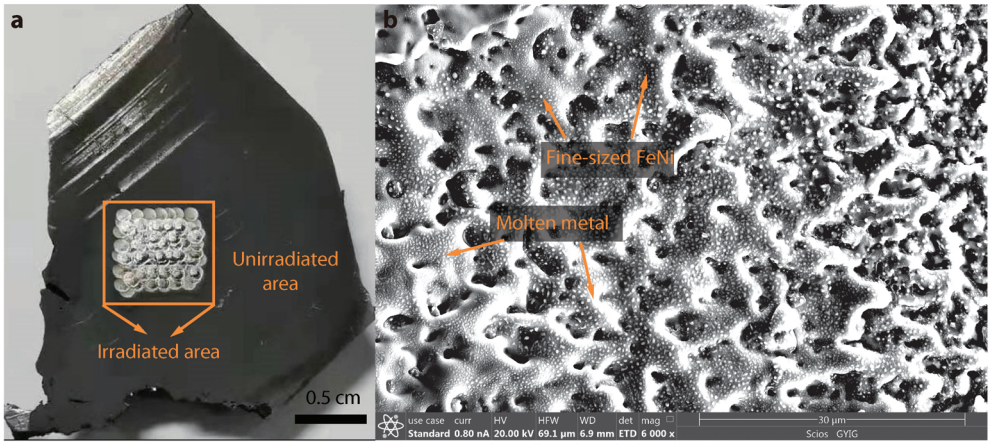

Fig. 5. Results of laser irradiation of IIIAB iron meteorite Dahongliuxia. (*a*) Photo of the unirradiated and irradiated area in Dahongliuxia. After irradiation, the original gray surface becomes brighter. (*b*) Secondary electron image of irradiated Dahongliuxia. A large number of fine-sized metal particles and melts are distributed in the irradiated area.

slope. In addition, even with a slight increase in the proportion of smooth planes, the spectrum changes significantly (Britt & Pieters 1988). Therefore, we are inclined to believe that the brightening and bluing of Dahongliuxia are caused by changes in surface roughness, which is different from our previously noticed SWSAE caused by composition changes (Zhang et al. 2022). The irradiated result of Dahongliuxia seems to indicate that asteroids with rough metallic surfaces may become smoother as well as spectrally brighter and bluer after micrometeoroid bombardments due to the melting-flowing-cooling effect of the metal. However, in contrast to the results from the laser irradiation of Dahongliuxia (which cannot bring new materials), the SWSAE and causes of natural metallic asteroids may be more complicated and are now poorly understood because: (1) materials from the impactors may cover the asteroid surfaces, altering the geometric albedo and the NIRS, as revealed by a high-speed impact simulation of silicates on iron meteorites (Libourel et al. 2019); and (2) the reflectance and spectral slope strongly depend on surface roughness and observation geometry (Britt & Pieters 1988; Cloutis et al. 2010) – however, we do not yet know the surface state of fresh metallic asteroids (e.g., whether their surfaces are dominated by slabs or fine-sized metallic regolith, along with what their surface roughness is and what the particle size of regolith is). In addition, we do not yet understand how micrometeoroid bombardments change surface composition and roughness. In the future, for metallic asteroids, more SW simulated experiments are strongly required and the surface state of fresh metallic asteroids should also be considered with care.

In summary, although we do not yet have very clear pictures of the surface of E- and M-type asteroids, the laser irradiation of these meteorites suggests that SW may be one of the important aspects contributing to the slope difference between aubrite (such as our Norton County) and E-type asteroids. Also, SW may play a role in blurring the boundaries of E- and M-type asteroids, resulting in a partial overlap of data points in Fig. 3.

4.2. Composition of M-type asteroids

In Sect. 3.3, we mention that M-type asteroids exhibit a wide NIRS range. Based on the spectral results of aubrite, ECs, and IMs (in Figs. 2c to f), if we ignore the differences in SW and the difference in particle size of regolith among M-type asteroids, the difference in NIRS among M-type objects probably

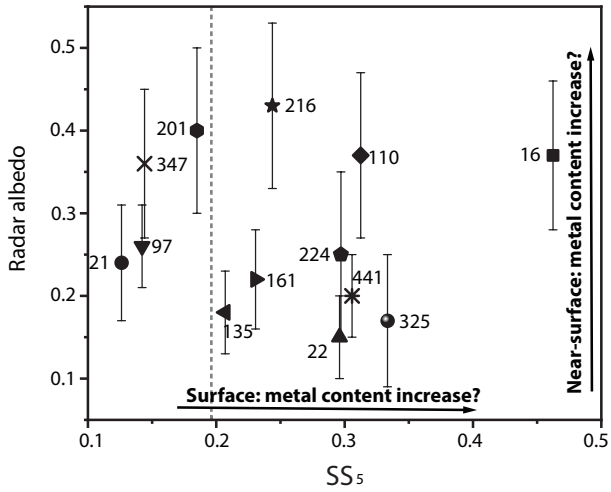

Fig. 6. Radar albedo and spectral slope calculated in 1.1–1.4 μm (SS_5) on M-type asteroids. The dashed line represents the upper limit of SS_5 of E-type asteroids (0.18693, the value of SS_5 of asteroid 2035 Stearn), which divides M-type into two parts: bodies with a low SS_5 fallen into the range of SS_5 of E-type (left side of the dashed line) and bodies with a higher SS_5 than E-type (right side of the dashed line).

reflect the relative content of metal (or enstatite) on the surface. As shown in Fig. 3d or Fig. 6, asteroids with the lowest SS_5 and overlapping with part of E-type asteroids (e.g., 21 Lutetia, 97 Klotho, 201 Penelope, and 347 Pariana) may indicate a metal-poor surface, consistent with EL meteorites; asteroids with the highest SS_5 (e.g., 16 Psyche) may indicate a metallic surface, consistent with IMs. As for the rest of the objects, 135 Hertha, 161 Athor, and 216 Kleopatra show a lower SS_5 and close to the SS_5 upper boundary of E-type asteroids (the dashed line in Fig. 6), indicating a potential metal-poorer surface (may be consistent with EL meteorites) than 22 Kalliope, 110 Lydia, 224 Oceana, 325 Heidelberga, 441 Bathilde, and 872 Holda (may be consistent with EH meteorites). By comparing the visible to infrared reflectance spectra (0.3–25 μm), 21 Lutetia was best linked to ECs by Vernazza et al. (2011); meanwhile, based on comparing the VIS-NIR reflectance spectra, 161 Athor was best linked to EL meteorites by Avdellidou et al. (2022). These two results are consistent with the results presented here. We have listed our inferred conclusions in Table 5.

Table 5. Properties and possible composition of M-type asteroids.

Number	Name	Density (g cm^{-3})	Radar albedo	SS_5	Potential main composition	Potential subsurface composition	Potential surface composition
16	Psyche	3.70±0.60–4.20±0.60$^{(aa)}$	0.37±0.09	0.46238	IMs	IMs or EH	IMs
21	Lutetia	3.45±0.21$^{(a)}$; 3.40±0.30$^{(b)}$	0.24±0.07	0.12613	ECs	ECs	EL
22	Kalliope	3.35±0.33–4.36±0.50$^{(bb)}$	0.15±0.05	0.29601	ECs or IMs	ECs	EH?
97	Klotho	4.16±0.62$^{(c)}$	0.26±0.05	0.14219	IMs	ECs	EL
110	Lydia	No data	0.37±0.10	0.31249	–	IMs or EH	EH?
135	Hertha	4.50±0.70$^{(d)}$	0.18±0.05	0.20695	IMs	ECs	EL?
161	Athor	No data	0.22±0.06	0.23059	–	ECs	EL?
201	Penelope	No data	0.40±0.10	0.18491	–	IMs or EH	EL
216	Kleopatra	3.38±0.50–5.00±0.70$^{(cc)}$	0.43±0.10	0.24372	ECs or IMs	IMs or EH	EL?
224	Oceana	No data	0.25±0.10	0.29717	–	ECs	EH?
325	Heidelberga	No data	0.17±0.08	0.33339	–	ECs	EH?
347	Pariana	No data	0.36±0.09	0.14411	–	IMs or EH	EL
441	Bathilde	No data	0.20±0.05	0.30583	–	ECs	EH?
872	Holda	No data	No data	0.32747	–	–	EH?

Notes. Density data are collected from $^{(a)}$Vernazza et al. (2021), $^{(b)}$Sierks et al. (2011), $^{(c)}$Carry (2012), $^{(d)}$Hanuš et al. (2017), $^{(aa)}$(Hanuš et al. 2017; Shepard et al. 2017; Viikinkoski et al. 2018; Drummond et al. 2018; Ferrais et al. 2020; Siltala & Granvik 2021; Vernazza et al. 2021), $^{(bb)}$(Descamps et al. 2008; Hanuš et al. 2017; Vernazza et al. 2021), $^{(cc)}$(Descamps et al. 2011; Hanuš et al. 2017; Marchis et al. 2021; Vernazza et al. 2021). Radar albedo data are collected from "Radar-detected asteroids with radar-measured parameters" database web (`http://www.johnstonsarchive.net/astro/radarasteroids.html`). "–" means the composition is unknown.

We note, however, that although we provide inferences on surface compositions in Table 5, these inferences are qualitative and empirical based on the relative highs and lows of SS_5 values, rather than by directly adopting S_5 boundaries among our different-type slab samples (as the dotted boxes we drew in Fig. 2e) to constrain asteroids. This is because: (1) almost all of our samples are slabs (slabs preserve in situ information and facilitate microscopic analysis) and M-type asteroids may develop regolith – with the average low radar circular-polarization ratio on M-type asteroids, 0.12, indicating that their surfaces may be dominated by fine-sized materials (Virkki et al. 2014), while the spectral slope is generally different between slabs and particles; (2) M-type asteroids may have been altered by SW processes, unlike our fresh slab meteorites; (3) our meteorites and asteroids have different observation geometries. These three factors should be considered very carefully when directly comparing the reflectance spectra of meteorites and asteroids.

Considering the sensibility of radar albedo to composition – for instance, M-type asteroids tend to show a higher value than C- and S-class bodies (Magri et al. 2007) – and the fact that the radar wave has a deeper penetration depth (reflecting the information of subsurface) than VIS-NIR light (only reflects the surface information), it may be able to better constrain the composition of M-type asteroids by combining radar albedo and SS_5. As shown in Fig. 6 and Table 5, five M-type asteroids (16 Psyche, 110 Lydia, 201 Penelope, 216 Kleopatra, and 347 Parina) show a higher radar albedo (>0.3), indicating they probably develop a more metal-rich subsurface (composed of IMs or EH) than the remaining nine bodies (radar albedo <0.3, indicating they may be composed of EH or EL).

In addition, because density is sensitive to metal content in meteorites, for example, ECs have a range of 3.15–3.78 g cm^{-3} (Macke et al. 2010), and iron meteorites change from 6.4 to 7.75 g cm^{-3} (Moore et al. 1999), M-type asteroids richer in metal are expected to have a higher density than metal-poorer bodies. Meanwhile, considering that asteroids generally have a higher porosity than meteorites, metallic asteroids probably have a lower density than IMs; that is to say, the density of parent bodies of ECs should not exceed 3.78 g cm^{-3} (the upper limit of ECs). Based on this, for M-type asteroids, here we try to give a rough constraint on the main composition. For 21 Lutetia, Sierks et al. (2011) and Vernazza et al. (2021) reported a density of 3.40±0.30 g cm^{-3} and 3.45±0.21 g cm^{-3}, respectively, indicating that ECs may dominate its main composition. 97 Klotho and 135 Hertha have a high density of 4.16±0.62 g cm^{-3} and 4.50±0.70 g cm^{-3} (all exceed 3.78 g cm^{-3}, see Table 5), respectively, implying that their main composition may be IMs. As for 16 Psyche, 22 Kalliope, and 216 Kleopatra, different studies have given a variety of results: 3.70±0.60 to 4.20±0.60 g cm^{-3} on 16 Psyche (Hanuš et al. 2017; Shepard et al. 2017; Viikinkoski et al. 2018; Drummond et al. 2018; Ferrais et al. 2020; Siltala & Granvik 2021; Vernazza et al. 2021), 3.35±0.33 to 4.36±0.50 g cm^{-3} on 22 kalliope (Descamps et al. 2008; Hanuš et al. 2017; Vernazza et al. 2021), and 3.38±0.50 to 5.00±0.70 g cm^{-3} on 216 Kleopatra (Descamps et al. 2011; Hanuš et al. 2017; Marchis et al. 2021; Vernazza et al. 2021). These results indicate that the potential main composition of 16 Psyche is IMs, while 22 Kalliope and 216 Kleopatra are mainly dominated by ECs (if their low-density estimations ~3.3 g cm^{-3} are true) or IMs (if their high-density estimations are true). Although 16 Psyche, 97 Klotho, and 135 Hertha have potential main metallic composition, none of them reach the density range of IMs, indicating the existence of porous structure or mixing non-metallic substances, or both. Due to the high radar albedo and SS_5, for 16 Psyche, we tend to support the porous structure scenario rather than "a mixing of non-metallic substances."

In summary, 16 Psyche shows high density and radar albedo, as well as the highest SS_5, indicating that it may be an object formed by the aggregation of residual metallic core fragments of differentiated planetesimals and as the source of IMs. Then, 21 Lutetia shows low density and radar albedo, as well as the

lowest SS_5, indicating that it may be a typical parent body of ECs. Thus, we suggest using the terms "Mm" and "Me" to represent them, respectively, as previously proposed by Shepard et al. (2010). Notably, 97 Klotho and 135 Hertha show a high density and a low radar albedo and SS_5, implying that they might represent an exciting species – namely, asteroids that still retain a metallic core and silicate mantle.

5. Conclusions

In this study, we measure and compare the visible and near-infrared reflectance spectra of aubrite, enstatite chondrites, and iron meteorites. The aubrite shows the lowest near-infrared slope, enstatite chondrites show a moderate near-infrared slope, and iron meteorites show the highest near-infrared slope. In addition, the EL chondrite is similar to aubrite on the spectral slope, and the area richer in enstatite shows a lower spectral slope than the area richer in metal in the enstatite chondrite. We thus conclude that the near-infrared slope is closely related to the relative proportion of metal and enstatite in their mixed system: more metal tends to show a higher (redder) near-infrared slope and vice versa.

A diagram plotted by reflectance and near-infrared slope, especially slope calculated in the 1.1–1.2 μm and 1.1–1.4 μm bands, are best to distinguish aubrite, enstatite chondrites, and iron meteorites. The diagram plotted by geometric albedo and near-infrared slope calculated in 1.1–1.4 μm is useful to distinguish E- and M-type asteroids.

Although rare studies of space weathering on E- and M-type asteroids, the laser irradiation for aubrite, enstatite chondrites, and iron meteorites suggest that micrometeoroid bombardments may be one of the important effects to alter the near-infrared slopes of E- and M-type asteroids, and to increase the difficulty of distinguishing parent bodies of enstatite chondrites and iron meteorites using spectroscopy.

For M-type asteroids, the combined use of near-infrared slope calculated in 1.1–1.4 μm band, radar albedo, and density provide insight into the composition of M-type asteroids at different depths. We conclude that 16 Psyche is a representative metallic asteroid, while 21 Lutetia is a typical parent body of enstatite chondrites.

Although we have noticed that the near-infrared slope is sensitive to the content of metal and enstatite in their mixed system, in this study, we cannot yet give an equation to quantitatively infer the proportion of metal (or enstatite) through the measured near-infrared slope. Next step, an experiment to measure the near-infrared slope of enstatite-metal mixtures with different proportions of metal will be performed, which will be expected to provide a reference to accurately predict the composition on surfaces of E- and M-type asteroids. In addition, considering that a good relationship between "the depth of the negative polarisation branch" and "the near-infrared slope" has been noticed by Belskaya et al. (2022) based on polarimetric observations, that is, the former increases with decreasing the latter, next step, it will be worth investigating the relationship between polarimetric parameters and metal content in our enstatite-mental mixed experiments.

Acknowledgements. The authors would like to thank Francesca E. DeMeo for a very beneficial discussion on asteroid taxonomy and space weathering effects, and thank Takahiro Hiroi and Cateline Lantz for a useful discussion on spectra of E-type asteroids. We also acknowledge Wenzhe Fa and Qinwei Zhang for helping to improve the original manuscript. In particular, the authors want to thank Pierre Beck for his excellent suggestions on spectral analysis data and discussions. Yang Li wants to thank funding support from the Strategic Priority Research Program of the Chinese Academy of Science grant XDB 41000000; the Youth Innovation Promotion Association CAS grant 2020395. Ziliang Jin wants to thank funding support from the Science and Technology Development Fund of Macao SAR 0067/2021/A.

References

Aines, R. D., & Rossman, G. R. 1984, J. Geophys. Res. Solid Earth, 89, 4059
Avdellidou, C., Delbo, M., Morbidelli, A., et al. 2022, A&A, 665, A9
Barucci, M. A., Fulchignoni, M., Fornasier, S., et al. 2005, A&A, 430, 313
Beck, P., Schmitt, B., Potin, S., Pommerol, A., & Brissaud, O. 2021, Icarus, 354, 114066
Bell, J. F., Davis, D. R., Hartmann, W. K., & Gaffey, M. J. 1989, Asteroids II, 921
Belskaya, I., Berdyugin, A., Krugly, Y., et al. 2022, A&A, 663, A146
Binzel, R. P., Harris, A. W., Bus, S. J., & Burbine, T. H. 2001, Icarus, 151, 139
Binzel, R. P., Birlan, M., Bus, S. J., et al. 2004, Planet. Space Sci., 52, 291
Bottke, W. F., Nesvornỳ, D., Grimm, R. E., Morbidelli, A., & O'Brien, D. P. 2006, Nature, 439, 821
Britt, D., & Pieters, C. 1994, Geochim. Cosmochim. Acta, 58, 3905
Britt, D., & Pieters, C. 1988, in Lunar and Planetary Science Conference Proceedings, 18, 503
Burbine, T., McCoy, T., Binzel, R., & Bus, S. 2001, Meteor. Planet. Sci. Suppl., 36, A31
Burns, R. G. 1970, Am. Mineral. J. Earth Planet. Mater., 55, 1608
Bus, S. J., & Binzel, R. P. 2002, Icarus, 158, 106
Carry, B. 2012, Planet. Space Sci., 73, 98
Chapman, C. R., & Salisbury, J. W. 1973, Icarus, 19, 507
Clark Jr, S. P. 1957, Am. Mineral. J. Earth Planet. Materi., 42, 732
Clark, R. N., & Roush, T. L. 1984, J. Geophys. Res. Solid Earth, 89, 6329
Clark, R. N., King, T. V., Klejwa, M., Swayze, G. A., & Vergo, N. 1990, J. Geophys. Res. Solid Earth, 95, 12653
Clark, B. E., Lucey, P., Helfenstein, P., et al. 2001, Meteor. Planet. Sci., 36, 1617
Clark, B. E., Bus, S., Rivkin, A., Shepard, M., & Shah, S. 2004a, AJ, 128, 3070
Clark, B. E., Bus, S. J., Rivkin, A. S., et al. 2004b, J. Geophys. Res. Planets, 109
Cloutis, E. A. 1989, Science, 245, 165
Cloutis, E. A., Gaffey, M. J., Smith, D. G., & Lambert, R. S. J. 1990, J. Geophys. Res. Solid Earth, 95, 281
Cloutis, E. A., Hardersen, P. S., Bish, D. L., et al. 2010, Meteor. Planet. Sci., 45, 304
DeMeo, F. E., & Carry, B. 2014, Nature, 505, 629
DeMeo, F. E., Binzel, R. P., Slivan, S. M., & Bus, S. J. 2009, Icarus, 202, 160
Descamps, P., Marchis, F., Pollock, J., et al. 2008, Icarus, 196, 578
Descamps, P., Marchis, F., Berthier, J., et al. 2011, Icarus, 211, 1022
Drummond, J. D., Merline, W. J., Carry, B., et al. 2018, Icarus, 305, 174
Ferrais, M., Vernazza, P., Jorda, L., et al. 2020, A&A, 638, A15
Fornasier, S., & Lazzarin, M. 2001, Icarus, 152, 127
Fornasier, S., Belskaya, I., Fulchignoni, M., Barucci, M., & Barbieri, C. 2006, A&A, 449, L9
Fornasier, S., Migliorini, A., Dotto, E., & Barucci, M. 2008a, Asteroids Comets Meteors, 1405, 8045
Fornasier, S., Migliorini, A., Dotto, E., & Barucci, M. 2008b, Icarus, 196, 119
Fornasier, S., Clark, B., Dotto, E., et al. 2010, Icarus, 210, 655
Gaffey, M. J., & Kelley, M. S. 2004, in Lunar and Planetary Science Conference, 1812
Gaffey, M. J., & McCord, T. 1979, Asteroids, 688
Gaffey, M. J., Reed, K. L., & Kelley, M. S. 1992, Icarus, 100, 95
Gradie, J., & Tedesco, E. 1982, Science, 216, 1405
Hanuš, J., Viikinkoski, M., Marchis, F., et al. 2017, A&A, 601, A114
Hardersen, P. S., Gaffey, M. J., & Abell, P. A. 2005, Icarus, 175, 141
Hardersen, P. S., Cloutis, E. A., Reddy, V., MOTHÉ-DINIZ, T., & Emery, J. P. 2011, Meteor. Planet. Sci., 46, 1910
Keil, K. 1968, J. Geophys. Res., 73, 6945
Keil, K. 1989, Meteoritics, 24, 195
Keil, K. 2010, Geochemistry, 70, 295
Keller, H., Barbieri, C., Koschny, D., et al. 2010, Science, 327, 190
Kimura, M., & Lin, Y. 1999, Antarctic Meteor. Res., 12, 1
Landsman, Z. A., Campins, H., Pinilla-Alonso, N., Hanuš, J., & Lorenzi, V. 2015, Icarus, 252, 186
Libourel, G., Nakamura, A. M., Beck, P., et al. 2019, Sci. Adv., 5, eaav3971
Lin, Y. 2022, Progr. Earth Planet. Sci., 9, 1
Lin, Y., Zhang, Y., Hu, S., et al. 2020, Space Sci. Rev., 216, 1
Macke, R. J., Consolmagno, G. J., Britt, D. T., & Hutson, M. L. 2010, Meteor. Planet. Sci., 45, 1513
Magri, C., Consolmagno, G. J., Ostrch, S. J., Benner, L. A., & Beeney, B. R. 2001, Meteor. Planet. Sci., 36, 1697

Magri, C., Nolan, M. C., Ostro, S. J., & Giorgini, J. D. 2007, Icarus, 186, 126
Marchis, F., Jorda, L., Vernazza, P., et al. 2021, A&A, 653, A57
Markus, K., Moroz, L., Arnold, G., et al. 2018, Planet. Space Sci., 159, 43
McCoy, T. J., Dickinson, T. L., & Lofgren, G. E. 1999, Meteor. Planet. Sci., 34, 735
McKay, D. S., Heiken, G., Basu, A., et al. 1991, Lunar Sourcebook, 567, 285
Moore, L., Flynn, G., & Klock, W. 1999, in Lunar and Planetary Science Conference, 1128
Mueller, M., Harris, A. W., & Fitzsimmons, A. 2007, Icarus, 187, 611
Nedelcu, D. A., Birlan, M., Vernazza, P., et al. 2007, A&A, 473, L33
Neeley, J., Clark, B., Ockert-Bell, M., et al. 2014, Icarus, 238, 37
Noble, S. K., Pieters, C. M., & Keller, L. P. 2007, Icarus, 192, 629
Ockert-Bell, M. E., Clark, B. E., Shepard, M. K., et al. 2008, Icarus, 195, 206
Ockert-Bell, M. E., Clark, B., Shepard, M., et al. 2010, Icarus, 210, 674
Ostro, S. J., Campbell, D., Chandler, J., et al. 1991, Science, 252, 1399
Penttilä, A., Martikainen, J., Gritsevich, M., & Muinonen, K. 2018, J. Quant. Spectrosc. Radiative Transfer, 206, 189
Pieters, C. M., & Noble, S. K. 2016, J. Geophys. Res. Planets, 121, 1865
Rayner, J., Toomey, D., Onaka, P., et al. 2003, PASP, 115, 362
Reddy, V., Sanchez, J. A., Bottke, W. F., et al. 2016, AJ, 152, 162
Reddy, V., Pearson, N., Agee, C., et al. 2019, in Lunar and Planetary Science Conference, 2132, 2212
Rivkin, A., Howell, E., Britt, D., et al. 1995, Icarus, 117, 90
Rivkin, A., Howell, E., Lebofsky, L., Clark, B., & Britt, D. 2000, Icarus, 145, 351
Rubin, A. E., & Keil, K. 1983, Earth Planet. Science Lett., 62, 118
Sasaki, S., Nakamura, K., Hamabe, Y., Kurahashi, E., & Hiroi, T. 2001, Nature, 410, 555
Scott, E. R. 2020, Oxford Research Encyclopedia of Planetary Science, 206
Shepard, M. K., Clark, B. E., Nolan, M. C., et al. 2008, Icarus, 195, 184
Shepard, M. K., Clark, B. E., Ockert-Bell, M., et al. 2010, Icarus, 208, 221
Shepard, M. K., Taylor, P. A., Nolan, M. C., et al. 2015, Icarus, 245, 38
Shepard, M. K., Richardson, J., Taylor, P. A., et al. 2017, Icarus, 281, 388
Sierks, H., Lamy, P., Barbieri, C., et al. 2011, Science, 334, 487
Siltala, L., & Granvik, M. 2021, ApJ, 909, L14
Takir, D., Reddy, V., Sanchez, J. A., Shepard, M. K., & Emery, J. P. 2016, AJ, 153, 31
Tedesco, E. F., Noah, P. V., Noah, M., & Price, S. D. 2002, AJ, 123, 1056
Tholen, D. J. 1984, PhD thesis, The University of Arizona
Veeder, G., Hanner, M., Matson, D., et al. 1989, AJ, 97, 1211
Vernazza, P., Lamy, P., Groussin, O., et al. 2011, Icarus, 216, 650
Vernazza, P., Ferrais, M., Jorda, L., et al. 2021, A&A, 654, A56
Viikinkoski, M., Vernazza, P., Hanuš, J., et al. 2018, A&A, 619, L3
Virkki, A., Muinonen, K., & Penttilä, A. 2014, Meteor. Planet. Sci., 49, 86
Watters, T. R., & Prinz, M. 1979, in Proceedings of the 10th Lunar and Planetary Science Conference
Wu, Y., Li, X., Yao, W., & Wang, S. 2017, J. Geophys. Res. Planets, 122, 1956
Zellner, B., Leake, M., Morrison, D., & Williams, J. 1977, Geochim. Cosmochim. Acta, 41, 1759
Zhang, H., Yang, Y., Jin, W., Liu, C., & Hsu, W. 2014, Opt. Express, 22, 21280
Zhang, P., Tai, K., Li, Y., et al. 2022, A&A, 659, A78

Appendix A: Sample description

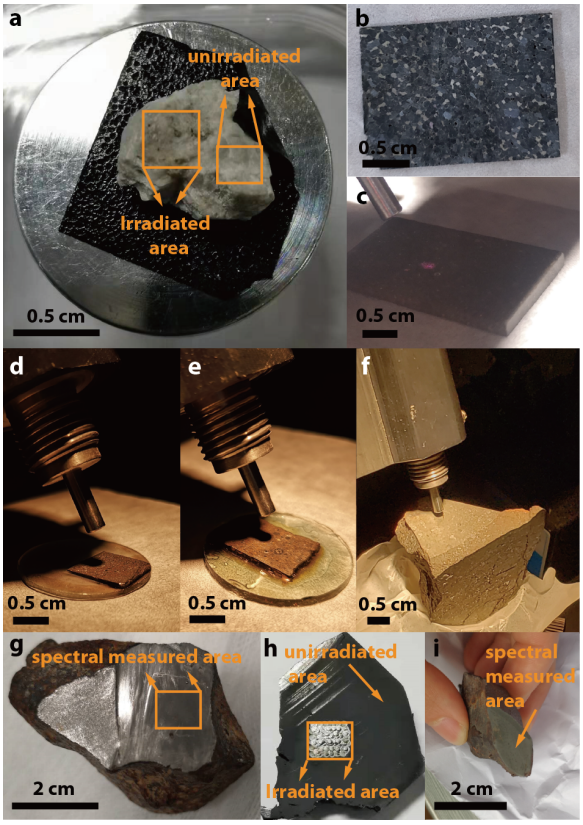

Fig. A.1. Photos of meteorites used in this study. (a) to (i) are Norton County, Itqiy, NWA 4945, Abee, Indarch, Qingzhen, Huoyanshan, Dahongliuxia, and Gebel Kamil, respectively.

Figure A.1 provides photos of all the meteorites used in this study, and the following describes the detailed information on the samples.

Norton County: Aubrite (enstatite achondrite) observed falling into the United States in 1948. Our sample is a fresh fragment. The mineralogy analysis shows that it is composed of 84.5 vol% enstatite ($En_{98.76}Fs_{0.10}Wo_{1.12}$), 10 vol% forsterite ($Fo_{99.99}$), 2.7 vol% diopside, 1 vol% plagioclase, 1 vol% troilite, and 0.3 vol% kamacite (Watters & Prinz 1979).
Itqiy: EH7 enstatite chondrite found in Western Sahara in 1990. Our sample is a fresh thin slab, and some fine-sized metal can be seen on the polished surface. The main minerals are 78 vol% enstatite ($En_{96.8}Fs_{0.2}Wo_{3.0}$, grain size 0.5-4 mm) and 22 vol% metal (grain size 0.2-2 mm; mineralogic description see Meteoritical Bulletin Database web[2]).
Qingzhen: EH3 enstatite chondrite observed falling into Qingzhen, Guizhou, China in 1976. Our sample is a fresh slab cut from a small block (block sample see Fig. A.1f), and scattered fine-sized metal can be seen on the polished surface. Our analysis suggests that the main mineral is enstatite ($En_{81-100}Fs_{0-18}$) followed by FeNi metal and troilite.
Abee: EH4 enstatite chondrite observed falling into North of Edmonton, Alberta, Canada in 1952. Our sample is a fresh thin slab, and a large amount of scattered fine-sized metal can be seen on the polished surface. Our analysis shows that the main mineral of Abee is enstatite ($En_{94.85-100}Fs_{0-5.14}$) followed by FeNi metal and troilite. The abundance of enstatite in different clasts is 22-41 wt%, in the matrix is 46-52 wt%, and in dark inclusion is 37 wt%; the content of FeNi metal in different clasts is 22-65 wt%, in the matrix is 20-30 wt%, and in dark inclusions is 6 wt% (Rubin & Keil 1983).
Indarch: EH4 enstatite chondrite observed falling into Azerbaijan in 1891. Our sample is a fresh thin slab, and a large number of scattered fine-sized metal fragments can be seen on the polished surface, like Abee. Our analysis shows that the main mineral is enstatite ($En_{86.88-100}Fs_{0.029}$) followed by FeNi metal and troilite.
NWA4945: EL6 enstatite chondrite found in Northwest Africa in 2007. Our sample is a fresh slab. The mineralogy is dominated by fine-sized aggregate composed of 74 vol% enstatite ($En_{98.2-98.5}Fs_{0.1-0.3}Wo_{1.5-1.4}$), 8 vol% kamacite, and 8 vol% Cr-bearing troilite (mineralogical description see Meteoritical Bulletin Database web).
Huoyanshan: IAB iron meteorite found in Xinjiang, China in 2016. Our sample is a block that looks like a fist. The mineral composition are Kamacite (3.4-7.3 wt% Ni), Taenite (typical M-type zoning with Ni content decreasing from 47.3 wt% at the rims to 16.5 wt% at the cores), and minor schreibersite (46.2-53.9 wt% Ni, 12.9-16.4 wt% P; mineralogical description see Meteoritical Bulletin Database web).
Dahongliuxia: IIIAB iron meteorite found in Xinjiang, China in 2016. Our sample is a fresh slab cut from a large block.
Gebel Kamil: Ungrouped iron meteorite found in Egypt in 2009. Our sample is a small block.

Appendix B: Spectral analysis

For meteorites, we mainly focus on investigating their reflectance and spectral slopes. As shown in the sketch Fig. B.1a, $R_{0.55}$ is the absolute reflectance at 0.55 μm, which represents the typical reflectance in the visible region. In Fig. B.1b, S_1 to S_6 are liner fitting spectral slopes (the green short lines) in six bands: 0.4-0.5 μm, 0.5-0.6 μm, 0.8-0.9 μm, 1.1-1.2 μm, 1.1-1.4 μm, and 1.6-1.8 μm, respectively. We chose these bands to calculate the spectral slope because we noticed that in these bands, for most meteorites and asteroids, there are generally no absorption features, and the spectral slope increases or decreases continuously.

Please note that in this study, we did not put our meteorites and asteroids in the same figure to directly compare their spectral slopes. This is because our samples generally are slabs (slabs preserve in-situ information and facilitate microscopic analysis) rather than powders, while asteroid surfaces generally are dominated by regolith, therefore, using the spectral slope range of slab meteorites to directly constrain asteroids is unscientific due to the size effects. In addition, although a useful method (could convert the $R_{0.55}$ of meteorites to geometric albedo) — aimed to establish the direct comparison on "ability to reflect sunlight" between meteorite samples and asteroids — has been proposed by Beck et al. (2021), which is based on powder samples rather than slabs, we hence did not convert the $R_{0.55}$ of our meteorites to geometric albedo and compare with asteroids.

[2] https://www.lpi.usra.edu/meteor/

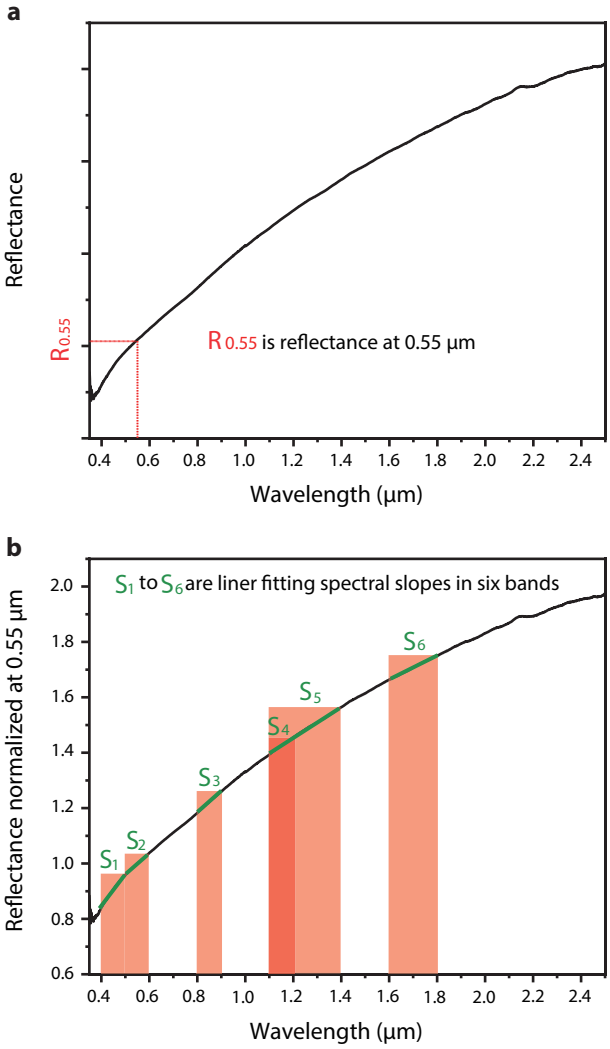

Fig. B.1. Sketch of spectral parameters of meteorites used in this study. (a) $R_{0.55}$ is the reflectance at 0.55 μm. (b) S_1 to S_6 are liner fitting spectral slopes in six bands: 0.4-0.5 μm, 0.5-0.6 μm, 0.8-0.9 μm, 1.1-1.2 μm, 1.1-1.4 μm, and 1.6-1.8 μm.